Acta Oceanol. Sin., 2021, Vol. 40, No. 5, P. 20–29
https://doi.org/10.1007/s13131-021-1808-0
http://www.hyxb.org.cn
E-mail: ocean2@hyxb.org.cn

Effects of westward shoaling pycnocline on characteristics and energetics of internal solitary wave in the Luzon Strait by numerical simulations

Haibin Lü[1, 2, 3, 4], Yujun Liu[1], Xiaokang Chen[1], Guozhen Zha[1], Shuqun Cai[2, 3, 5, 6*]

[1] Jiangsu Key Laboratory of Marine Bioresources and Environment/Jiangsu Key Laboratory of Marine Biotechnology, Jiangsu Ocean University, Lianyungang 222005, China

[2] State Key Laboratory of Tropical Oceanography, South China Sea Institute of Oceanology, Chinese Academy of Sciences, Guangzhou 510301, China

[3] Southern Marine Science and Engineering Guangdong Laboratory (Guangzhou), Guangzhou 511458, China

[4] Jiangsu Institute of Marine Resources Development, Lianyungang 222005, China

[5] University of Chinese Academy of Sciences, Beijing 100049, China

[6] Innovation Academy of South China Sea Ecology and Environmental Engineering, Chinese Academy of Sciences, Guangzhou 510301, China

Received 29 March 2020; accepted 29 December 2020

Abstract

An internal gravity wave model was employed to simulate the generation of internal solitary waves (ISWs) over a sill by tidal flows. A westward shoaling pycnocline parameterization scheme derived from a three-parameter model was adopted, and then 14 numerical experiments were designed to investigate the influence of the pycnocline thickness, density difference across the pycnocline, westward shoaling isopycnal slope angle and pycnocline depth on the ISWs. When the pycnocline thickness on both sides of the sill increases, the total barotropic kinetic energy, total baroclinic energy and ratio of baroclinic kinetic energy (KE) to available potential energy (APE) decrease, whilst the depth of isopycnal undergoing maximum displacement and ratio of baroclinic energy to barotropic energy increase. When the density difference on both sides of the sill decreases synchronously, the total barotropic kinetic energy, ratio of baroclinic energy to barotropic energy and total baroclinic energy decrease, whilst the depth of isopycnal undergoing maximum displacement increases. When the westward shoaling isopycnal slope angle increases, the total baroclinic energy increases whilst the depth of turning point almost remains unchanged. When the depth of westward shoaling pycnocline on both sides of the sill reduces, the ratio of baroclinic energy to barotropic energy and total baroclinic energy decrease, whilst the total barotropic kinetic energy and ratio of KE to APE increase. When one of the above four different influencing factors was increased by 10% while the other factors keep unchanged, the amplitude of the leading soliton in ISW Packet A was decreased by 2.80%, 7.47%, 3.21% and 6.42% respectively. The density difference across the pycnocline and the pycnocline depth are the two most important factors in affecting the characteristics and energetics of ISWs.

Key words: internal solitary waves, baroclinic energy, South China Sea, pycnocline

Citation: Lü Haibin, Liu Yujun, Chen Xiaokang, Zha Guozhen, Cai Shuqun. 2021. Effects of westward shoaling pycnocline on characteristics and energetics of internal solitary wave in the Luzon Strait by numerical simulations. Acta Oceanologica Sinica, 40(5): 20–29, doi: 10.1007/s13131-021-1808-0

1 Introduction

Internal solitary waves (ISWs) are important dynamic phenomena, usually generated by a tidally driven flow over submerged variable topography in a stratified ocean. It is expected that internal wave activity would increase in the northeastern South China Sea (SCS) through the 21st century because of the warming in the upper 100 m of the ocean since 1900 (DeCarlo et al., 2015). ISWs in the northeastern SCS evolve out of the internal tide generated in the Luzon Strait (Li et al., 2013; Zhao, 2014), where two underwater sea ridges, namely Lan-Yu Ridge to the east and Heng-Chun Ridge to the west, are located (Zheng et al., 2007; Du et al., 2008; Wang et al., 2012; Cao et al., 2017; Bai et al.,

Foundation item: The Key Research Program of Frontier Sciences, Chinese Academy of Sciences (CAS) under contract No. QYZDJ-SSW-DQC034; the Talent Project from Southern Marine Science and Engineering Guangdong Laboratory (Guangzhou) under contract No. GML2019ZD0304; the National Natural Science Foundation of China (NSFC) under contract Nos 41521005 and 62071207; the Priority Academic Program Development of Jiangsu Higher Education Institutions (PAPD); the Natural Science Foundation of Huai Hai Institute of Technology under contract No. Z2017006; the Project from Department of Natural Resources of Guangdong Province under contract No. (2020)017; the Open Project of State Key Laboratory of Tropical Oceanography, South China Sea Institute of Oceanology, CAS under contract No. LTO1702; Postgraduate Research & Practice Innovation Program of Jiangsu Province under contract No. SJCX19_0963.

*Corresponding author, E-mail: caisq@scsio.ac.cn

2017). ISWs induce strong convergence and divergence of horizontal current velocity with enormous energy during their propagations (Huang et al., 2014; Xu et al., 2016; Grimshaw et al., 2016; Chen et al., 2018).

On their path across the northeastern SCS, ISWs may undergo numerous transformations, and their propagation characteristics and energetics are bound to change because of various background environments, such as tidal flow over submerged topography (Chen et al., 2013), background shear current (Cai et al., 2008; Lü et al., 2016), mesoscale eddies (Xie et al., 2015), density stratification (Chen et al., 2014) and Kuroshio intrusion (Park and Farmer, 2013).

The effects of various background elements on the ISWs over the sea ridge are typically studied based on a density stratification with a horizontal uniform and vertically varying buoyancy frequency, namely $N(z)$. However, this kind of pycnocline assumption is not always applicable to actual oceanic conditions, especially in the Luzon Strait. In fact, the westward shoaling pycnocline coincides with a hydrostatic, geostrophic Kuroshio Current, situated between the west and east ridges in the Luzon Strait along a zonal transect at 20.75°N (Buijsman et al., 2010). Figure 1 shows that the pycnocline depth decreases westward from a total mean of (324±37) m at 123°E to (178±37) m at 119°E based on temperature profile data from January 1980 to December 1999 provided by the National Oceanographic and Atmospheric Administration (NOAA) and National Oceanographic Data Center (NODC) (Boyer and Levitus, 1994). For an ISW propagating along a shoaling pycnocline, its amplitude would be modulated by the pycnocline (Zheng et al., 1998). There is a conspicuous seasonal variation of the westward shoaling pycnocline with different slope angles in the Luzon Strait. The slope angle in December (Series 12 in Fig. 1) appeared larger than that in July. The shoaling pycnocline with a specific gradient had a significant effect on the internal waves in the ocean, which appeared on many continental margins (Osborne and Burch, 1980; Vázquez et al., 2008; Chen et al., 2007; Li et al., 2013; Bai et al., 2017). It is reported that the ISWs are affected when propagating through variable background hydrology and currents (Liu et al., 2017). However, little attention has been paid to the effects of westward shoaling pycnocline stratification on the characteristics and energetics of the generated ISWs in the Luzon Strait.

In this paper, large amplitude ISWs generated by tidal flows over submarine topography were investigated by using an internal gravity wave (IGW) model (Lamb, 2010). This investigation focused on the effect of westward shoaling pycnocline on characteristics and energetics of ISWs in the Luzon Strait. The model description, choice of model parameters and design of westward shoaling pycnocline are described in Section 2. In Section 3, the experimental results are shown and discussed. Finally, the conclusions are summarized in Section 4.

2 Model description

2.1 *Dynamic model and validation*

In this study, the IGW model was used, which is a 2.5 dimensional, non-hydrostatic nonlinear model. This numerical model has been successfully used to study a series of ISW generation problems (Lamb, 2010; Lamb and Kim, 2012). Sigma-coordinates are used in this two dimensional system. (x, z) are the horizontal and vertical coordinates, where x is positive to the east. The sea surface is at z=0, where z is positive upward. Under the rigid-lid, Boussinesq, inviscid and traditional f-plane approximations, the governing equations are shown as follows:

$$U_t + U\cdot\nabla U - fv\hat{i} = -\frac{1}{\rho_0}\nabla p - \frac{\rho}{\rho_0}g\hat{k}, \tag{1}$$

$$v_t + U\cdot\nabla v + fu = 0, \tag{2}$$

$$\rho_t + U\cdot\nabla\rho = 0, \tag{3}$$

$$\nabla\cdot U = 0, \tag{4}$$

where U=(u, w) is the velocity vector in the x, z-plane; u (x, z, 0) and w (x, z, 0) are the velocities at the initial time and they are set to zero; v is the velocity in the y direction; ρ and p are the density and pressure; g is the gravitational acceleration; $\hat{i}$ and $\hat{k}$ are the unit vectors in the x and z directions, respectively; and ρ_0=

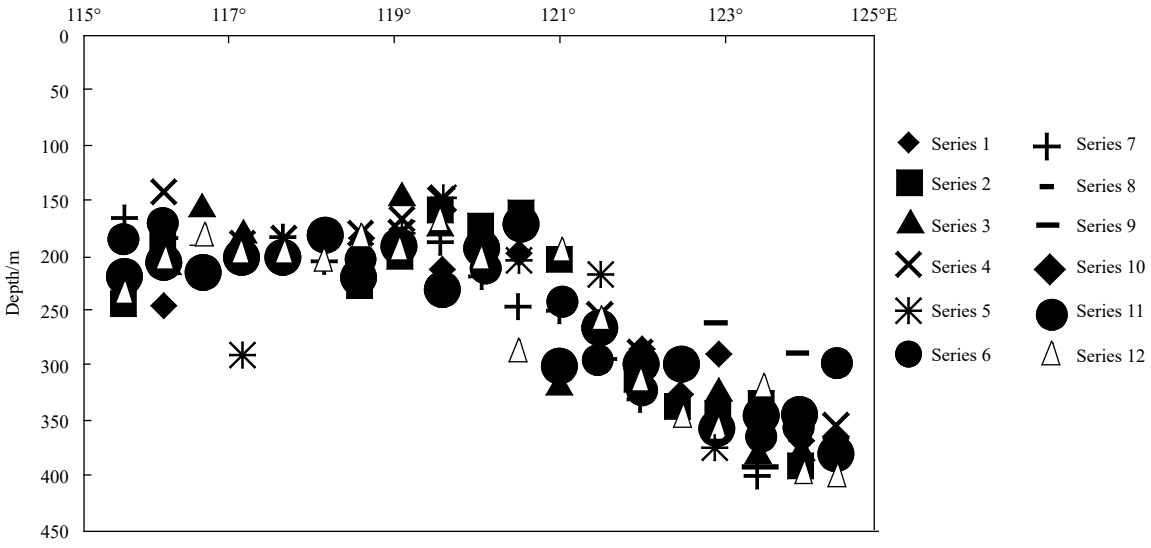

Fig. 1. A zonal distribution of pycnocline depth near the Luzon Strait adapted from Zheng et al. (2008). Series 1 represents the monthly mean pycnocline depth in January, Series 2 in February and so on.

1 000 kg/m^3 is the reference density. The Coriolis parameter is f=5.12×10^{-5} rad/s, which corresponds to a latitude of 20.75°N. A rigid lid at the surface z=0 and terrain following coordinates are used. Details of the IGW model have been provided by Lamb and Kim (2012).

The submerged variable sill is designed by

$$H(x) = -[H_0 - h_0\exp(-x^2/W^2)], \tag{5}$$

where h_0=530 m is the height of ridge, H_0=800 m is the water depth and W=5 km is the width of ridge. The choice of these parameters is to reflect the real situation of the Luzon Strait basically and resolve the distinct variation of the simulated ISWs. The computational domain extends from x=–L to L (here, L is 300 km), which is sufficiently long that no perturbations can reach the boundary. At the right boundary of the computational domain, the M_2 barotropic tidal flow with a maximum velocity of u_0=0.25 m/s and a tidal period T of 12.4 h are prescribed, while a radiation condition is applied at the left boundary. In all simulations, the horizontal spatial resolution is about 100 m, and there are 82 levels in vertical direction. The maximum time step is 20 s, and a variable time step is applied to satisfy the Courant-Friedrichs-Lewy condition.

Wang (2006) proposed a horizontal uniform density stratification based on a three-parameter model as defined by Eq. (6) in Fig. 2, which has been successfully used as the horizontal uniform and vertically varying stratification.

$$\rho_{\mathrm{a}}(z) = \exp\left\{\frac{\Delta\rho_{\mathrm{a}}}{2\rho_0}\tanh\left[\frac{-2(z+d)}{\delta}\right]\right\}, \tag{6}$$

where $\Delta\rho_{\mathrm{a}}$ is the density difference across the pycnocline, d is the pycnocline depth and δ is the pycnocline thickness.

The westward shoaling pycnocline was defined by Eq. (7):

$$\begin{aligned}\rho(x,z) =& \rho_0\{\tilde{\rho}_{\mathrm{l}}(z)[1-\tanh(x/R)] + \tilde{\rho}_{\mathrm{r}}(z)\times \\ & [1+\tanh(x/R)]\}, \quad R\neq 0,\end{aligned} \tag{7}$$

where $\tilde{\rho}_{\mathrm{l}}(z)$ and $\tilde{\rho}_{\mathrm{r}}(z)$ are calculated based on Eq. (6) on the west and east boundaries, respectively. R is half of the horizontal distance of the westward shoaling pycnocline in Fig. 3. To balance the shoaling pycnocline structure, the initial velocity fields could be self-adjusted based on the thermal wind balance relation $f\dfrac{\partial v}{\partial z} = -\dfrac{g}{\rho_0}\dfrac{\partial \rho}{\partial x}$ in the IGW model.

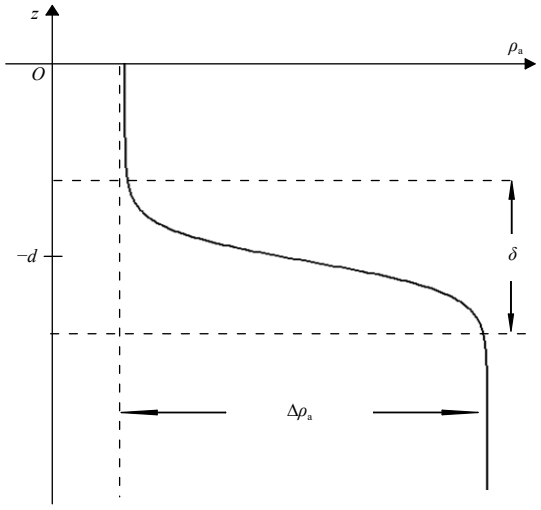

Fig. 2. Initial density derived from a three-parameter model adapted from Chen et al. (2014).

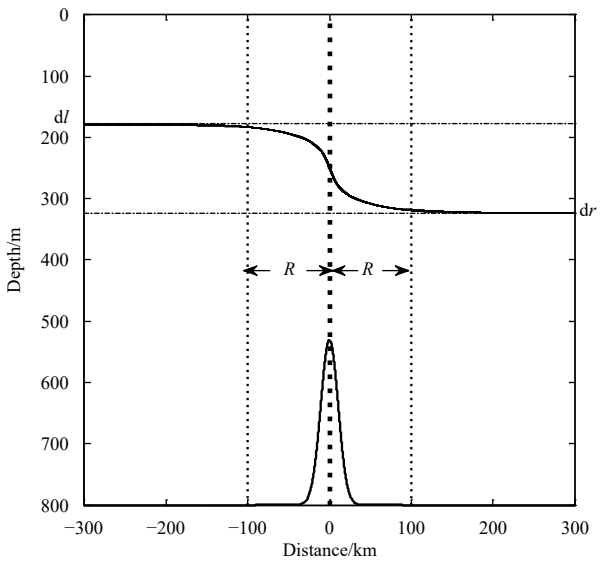

Fig. 3. Distribution of the initial density isolines in experiment E2 (the thick dotted line denotes the location of the horizontal center position of shoaling pycnocline).

An ISW packet was observed to the northeast of the Dongsha Islands on June 24, 2009 based on the shipboard X-band, thermistor chains and acoustic doppler current profilers (Lü et al., 2010). In fact, the IGW model has been well applied in the numerical simulations of ISWs (Lamb and Kim, 2012; Lü et al., 2016; Bai et al., 2017). Therefore, in the following study, 14 experiments are designed to study the sensitivity of the generated ISW to the changes of the westward shoaling pycnocline.

Fourteen experiments (E0–E13) are designed with the westward shoaling pycnocline derived from the three-parameter model by Eq. (6), but it is noted that the stratification in Experiment E0 is set to be horizontal uniform. For example, in Experiment E2, the westward shoaling pycnocline is shown in Fig. 3, and distributions of buoyancy frequency N vs. depth at the eastern and western parts are depicted in Fig. 4. R is half of the horizontal distance of the westward shoaling pycnocline, and dl (dr) is the pycnocline depth on the left (right), where the maximum of the vertical buoyancy frequency ($N_{\max}$) is shown.

In the following, the sensitivity of the generated ISW to changes of the westward shoaling pycnocline was investigated by combinations as follows: (1) influence of existence of westward shoaling pycnocline (E0 with Ei (i=1, 2, ···, 13)); (2) the increment of pycnocline thickness (E1, E2 and E3). The other conditions in experiments E2 and E3 are the same as those in experiment E1 except that δ is changed into 140 m and 200 m, respectively; (3) the density difference across the pycnocline is decreased (E1, E4 and E5). The other conditions in experiments E4 and E5 are the same as those in experiment E1 except that $\Delta\rho_{\mathrm{a}}$ is changed into 3 kg/m^3 and 2.5 kg/m^3, respectively; (4) isopycnal slope angle is increased (E6, E1 and E7). The other conditions in experiments E6 and E7 are the same as those in experiment E1 except that R is changed into 60 km and 140 km, respectively; (5) vertical depth of westward shoaling pycnocline is reduced (E9, E1 and E8). The other conditions in experiments E9 and E8 are the same as those in experiment E1 except that the vertical depths of westward

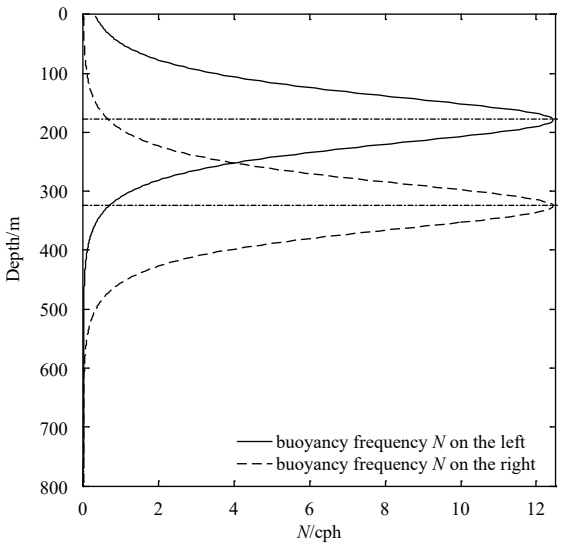

Fig. 4. Distributions of buoyancy frequency N vs. depth in Experiment E2.

shoaling pycnocline are increased by 30 m in experiment E9 and decreased by 60 m in E8; and (6) importance of different influencing factors (E1, E10–E13). Based on experiment E1, each influencing factor is increased by 10% in experiments Ei (E10–E13), respectively. For example, δ is changed into 89.1 m in E10, $\Delta\rho_a$ is changed into 4.4 kg/m^3 in E11, R is changed into 110 km in E12 and the vertical depth of westward shoaling pycnocline is increased by 10% in E13. The detailed setting of the 14 experiments used in this study is presented in Table 1. Note that in all experiments, the horizontal center position of the shoaling pycnocline just lies over the top of the submerged ridge.

2.2 *Wave energetics*

The baroclinic available potential energy (APE) and kinetic energy (KE) in a closed finite domain can be defined as (Lamb, 2008)

$$\mathrm{APE}=\int_{x_l}^{x_r}\int_{-H(x)}^{0}E_a\mathrm{d}z\mathrm{d}x, \tag{8}$$

and

$$\mathrm{KE}=\int_{x_l}^{x_r}\int_{-H(x)}^{0}E_k\mathrm{d}z\mathrm{d}x, \tag{9}$$

where x_r–x_l represents an integration distance across a steady wave packet, E_k is the baroclinic KE density given by

$$E_k(x,z,t)=0.5\rho(x,z,t)\left[(u')^2+(v')^2+(w')^2\right], \tag{10}$$

where the baroclinic velocity $u'=u-\dfrac{1}{H-h(x)}\displaystyle\int_{-H}^{0}u\mathrm{d}z$, $v'=v-\dfrac{1}{H-h(x)}\displaystyle\int_{-H}^{0}v\mathrm{d}z$, $w'=w-\dfrac{1}{H-h(x)}\displaystyle\int_{-H}^{0}w\mathrm{d}z$.

E_a is the APE density given by

$$E_a(x,z,t)=g\int_{z}^{z^*}[\bar{\rho}(s)-\rho(x,z,t)]\mathrm{d}s, \tag{11}$$

where $z^*(x, z, t)$ is the height of the fluid parcel at (x, z) at time t in the reference state and $\bar{\rho}$ is the initial undisturbed density (Lamb, 2008).

The total barotropic energy E_{k0} was defined by Lamb (2010):

$$E_{k0}=\int_{x=x_l}^{x_r}\int_{z=0}^{H}\frac{1}{2}\rho(x,z,t)[\bar{u}(z)+\bar{v}(z)]\mathrm{d}x\mathrm{d}z, \tag{12}$$

where $\bar{u}(z)$, $\bar{v}(z)$ are the vertical averaged speeds in the x, y-plane respectively. x_l, x_r represent the locations of the wavefront of leading ISW and the wave tail of the last ISW in a wave Packet A, which are also the left and right boundaries of the integral domain.

3 Results and discussion

A standard experiment E0 with a horizontal uniform and vertically varying stratification is designed with $\Delta\rho_a$=4 kg/m^3, d=

Table 1. Detailed setting of parameters for all experiments

Experiment	R/km	$\Delta\rho_a$/(kg·m^{-3})	N_{max}/s^{-1}	dl/m	dr/m	δ/m
E0	–	4.0	0.009 70	178.0	178.0	81.0
E1	100	4.0	0.009 70	178.0	324.0	81.0
E2	100	4.0	0.007 40	178.0	324.0	140.0
E3	100	4.0	0.006 20	178.0	324.0	200.0
E4	100	3.0	0.008 40	178.0	324.0	81.0
E5	100	2.5	0.007 70	178.0	324.0	81.0
E6	60	4.0	0.009 70	178.0	324.0	81.0
E7	140	4.0	0.009 70	178.0	324.0	81.0
E8	100	4.0	0.009 70	118.0	264.0	81.0
E9	100	4.0	0.009 70	208.0	354.0	81.0
E10	100	4.0	0.009 70	178.0	324.0	89.1
E11	100	4.4	0.009 70	178.0	324.0	81.0
E12	110	4.0	0.009 70	178.0	324.0	81.0
E13	100	4.0	0.009 70	195.8	341.8	81.0

Note: – represents no data. R is half of the horizontal distance of the westward shoaling pycnocline, $\Delta\rho_a$ is density difference across the pycnocline, N_{max} is the maximum of the buoyancy frequency, dl and dr are the pycnocline depth on the left and right sides of the sill respectively, and δ is the pycnocline thickness.

–178 m, and δ=81 m (Table 1). The effects of westward shoaling pycnocline on characteristics and energy conversion of the first ISWs in wave Packet A in experiment Ei (i=0, 1, ⋯, 13) at the fourth tidal period are summarized in Tables 2 and 3, and the density fields of the generated ISWs are shown in Fig. 5.

3.1 *Influence of pycnocline thickness (E1, E2 and E3)*

The influence of increased pycnocline thickness was studied by comparing the results in Fig. 6. Firstly, it showed that, when the pycnocline thickness was increased from 81 m in experiment E1 to 140 m in experiment E2 and 200 m in experiment E3, respectively, the depth of isopycnal undergoing maximum displacement and ratio of baroclinic energy to barotropic energy increased, whilst the ISW amplitude, number of ISWs, phase speed of ISWs, total barotropic kinetic energy, total baroclinic energy and ratio of KE to APE in Packet A decreased (Tables 2, 3 and Fig. 6). That was likely caused by the weakened stratification with increasing pycnocline thickness. Compared with experiment E1, $N_{\max}$ in experiments E2 and E3 were reduced by 23.71% and 36.08%, respectively. Secondly, if the pycnocline thickness was increased to 60 m (i.e., 0.075 of the total depth), then the depth of turning point changes was shallower (Fig. 6), which is –311 m in experiment E1, –299 m in experiment E2 and –284 m in experiment E3. Compared with experiment E1, the depths of turning points in experiments E2 and E3 were reduced by 3.90% and 8.70%, respectively. Thirdly, the decrease in horizontal baroclinic velocity at the depth of the pycnocline in experiment E1 is likely due to the influence of the increased pycnocline thickness (Fig. 6).

3.2 *Influence of density difference ($\Delta\rho_a$) (E1, E4 and E5)*

The density difference across the pycnocline has an important effect on the energetics of the ISWs in a horizontal uniform stratification (Chen et al., 2014). The influence of the density difference across the pycnocline in the westward shoaling pycnocline stratification on the ISWs was studied by comparing the results among experiments Ei (i=1, 4, 5) in Fig. 7. Firstly, it showed that when the density difference was reduced to 4 kg/m^3 in ex-

Table 2. Characteristics and energy conversion of the ISWs Packet A in experiments Ei (i=1, 2, ⋯, 13) at 4T

Experiment	ISW amplitude η/m	Depth of max displacement h_0/m	Number of ISWs	Location of ISWs S/km	Phase speed of ISWs C/(m·s^{-1})	Total barotropic kinetic energy E_{k0}/(MJ·m^{-1})	Ratio of baroclinic energy to barotropic energy	Total energy of APE and KE/(MJ·m^{-1})	Ratio of KE and APE (KE/APE)
E0	175.54	164	7	–132.39	0.878	10.925	0.160	1.752	0.587
E1	169.26	172	5	–126.19	0.896	6.776	0.181	1.226	0.640
E2	168.84	172	4	–121.49	0.842	5.957	0.199	1.184	0.623
E3	165.92	180	3	–116.99	0.789	5.267	0.206	1.085	0.606
E4	158.76	172	3	–108.69	0.717	5.191	0.140	0.728	0.615
E5	143.43	180	3	–98.69	0.645	4.654	0.099	0.458	0.619
E6	170.15	172	6	–126.99	0.896	8.088	0.171	1.383	0.632
E7	173.00	172	4	–125.89	0.860	6.986	0.174	1.216	0.631
E8	179.79	116	5	–118.19	0.824	8.171	0.120	0.982	0.649
E9	166.54	196	4	–129.39	0.896	5.799	0.245	1.419	0.620
E10	170.62	172	5	–125.59	0.877	6.210	0.194	1.206	0.641
E11	162.42	172	5	–132.59	0.931	6.981	0.208	1.452	0.642
E12	169.90	172	4	–126.09	0.877	6.596	0.178	1.176	0.648
E13	164.27	188	4	–128.09	0.877	5.596	0.163	0.910	0.668

Table 3. Effects of changes in westward shoaling pycnocline on the characteristics and energy conversion of the generated ISWs Packet A

Variation of westward shoaling pycnocline	Experiment pairs	ISW amplitude	Depth of isopycnal undergoing maximum displacement	Number of ISWs	Phase speed of ISWs	Total barotropic kinetic energy	Ratio of baroclinic energy and barotropic energy	Total energy of APE and KE	Ratio of KE and APE (KE/APE)
Pycnocline thickness is increased	(E1, E2)	–		–	–	–	+	–	–
	(E2, E3)	–	+	–	–	–	+	–	–
	(E1, E3)	–	+	–	–	–	+	–	–
Density difference across the pycnocline is reduced	(E1, E4)	–	+	–	–	–	–	–	–
	(E4, E5)	–	+		–	–	–	–	+
	(E1, E5)	–	+	–	–	–	–	–	–
Isopycnal slope angle is increased	(E7, E1)	–		+	+	–	+	+	+
	(E7, E6)	–		+	+	+	–	+	+
	(E1, E6)	+		+	+	+	–	+	–
Vertical depth of westward shoaling pycnocline is reduced	(E1, E8)	+	–		–	+	–	–	+
	(E9, E8)	+	–	+	–	+	–	–	+
Westward shoaling pycnocline is considered	(E0, Ei, i=1, 2, ⋯, 13)	– (except in E8)	+ (except in E8)	–		–		–	+

Note: the symbol +/– denotes an increase/decrease of the parameters, while blank cell denotes no significant variation.

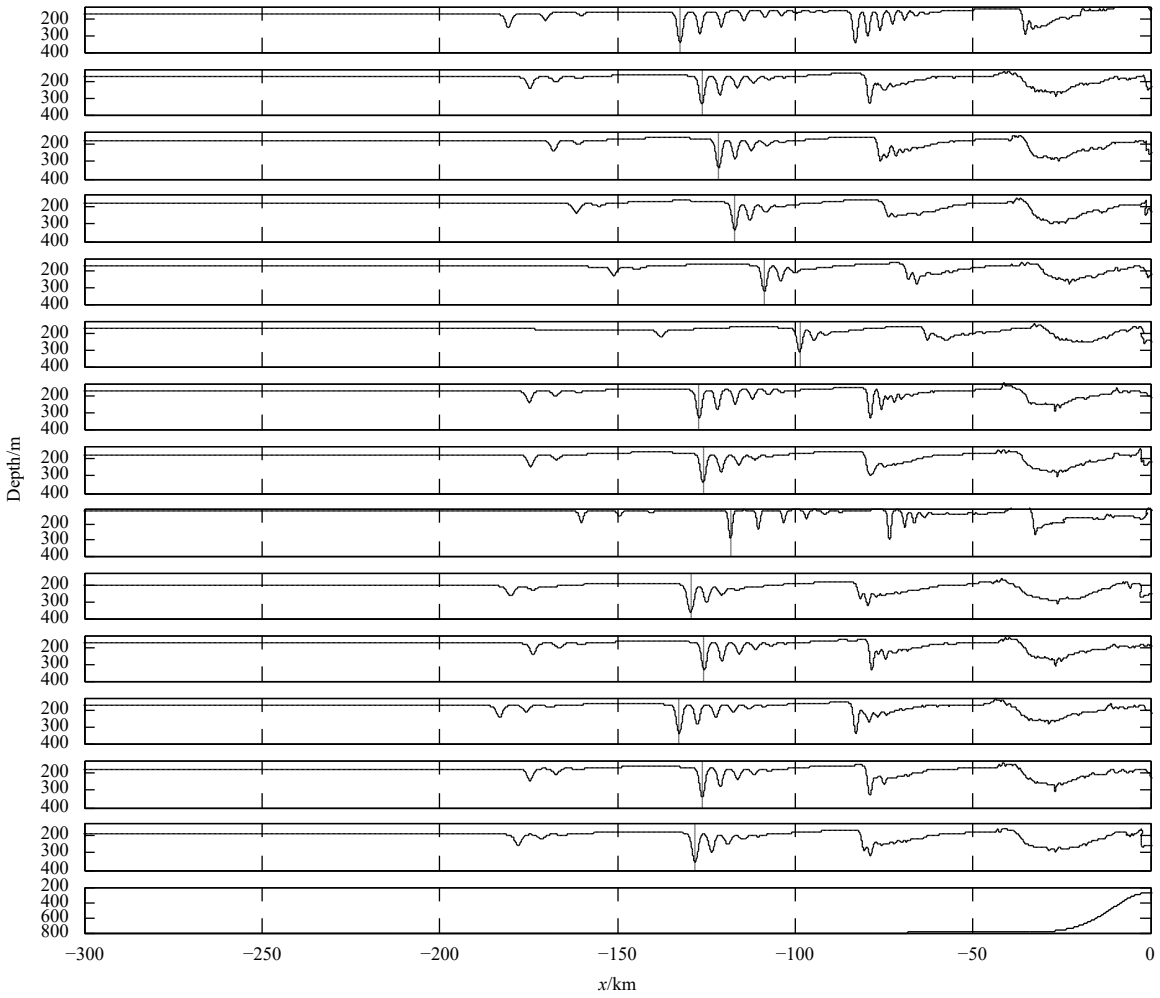

Fig. 5. Distribution of the density field after running four tidal periods in experiments E*i* (*i*=0, 1, ···, 13), respectively (where only the density isoline ρ=1 023.3 kg/m^3 is shown and the dashed line denotes the location of the trough of leading ISW in the wave Packet A).

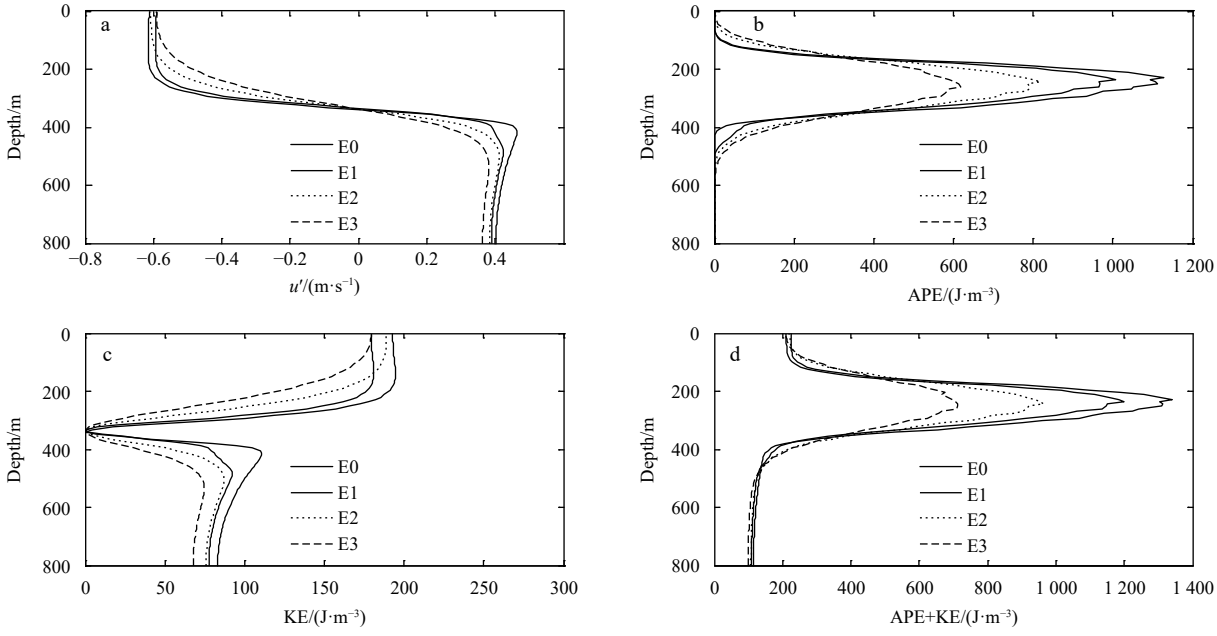

Fig. 6. Comparison of the model results along the dashed line section denoted in Fig. 5 in experiments E*i* (*i*=0, 1, 2, 3). a. Horizontal baroclinic velocity *u*′ vs. depth; b. APE densities vs. depth; c. KE densities vs. depth; d. APE+KE vs. depth.

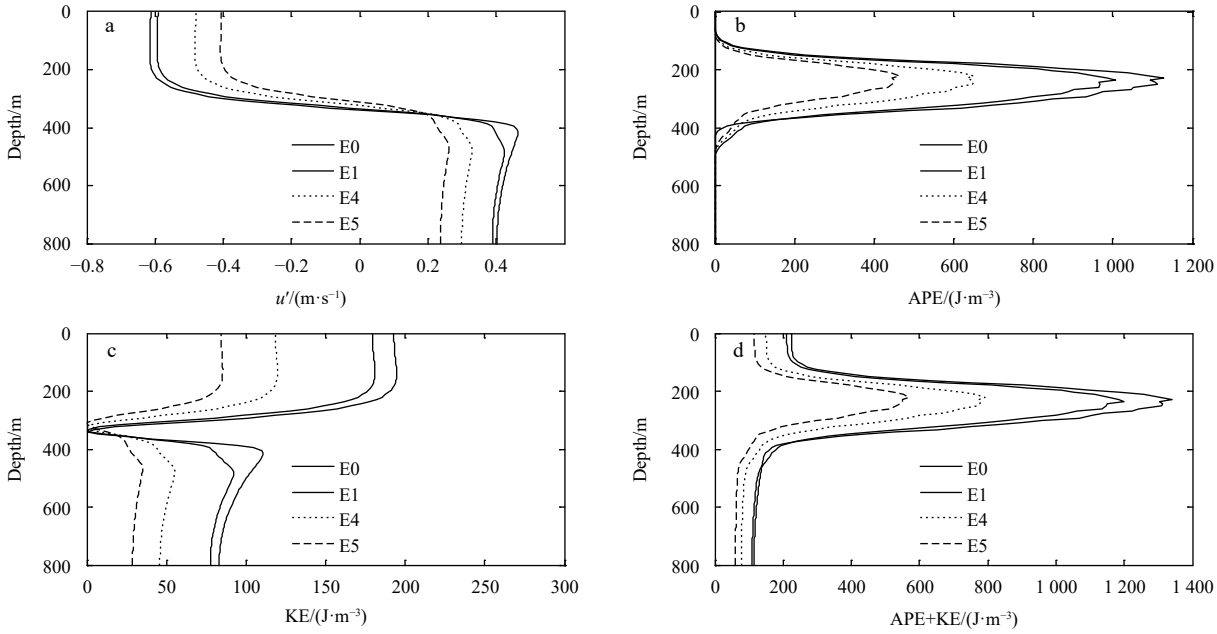

Fig. 7. Comparison of the model results along the dashed line section denoted in Fig. 5 in experiments E*i* (*i*=0, 1, 4, 5). a. Horizontal baroclinic velocity *u*′ vs. depth; b. APE densities vs. depth; c. KE densities vs. depth; d. APE+KE vs. depth.

periment E1, 3 kg/m^3 in experiment E4 and 2.5 kg/m^3 in experiment E5, respectively, the ISW amplitude, phase speed of ISWs, total barotropic kinetic energy, ratio of baroclinic energy to barotropic energy and total baroclinic energy in Packet A decreased, whilst the depth of isopycnal undergoing maximum displacement increased (Tables 2, 3 and Fig. 7). The energy decrease in ISWs with the weakened stratification is consistent with the conclusion by Chen et al. (2014). Secondly, if the density difference across the pycnocline was reduced, then the depth of turning point became shallower (Fig. 7a), i.e., the depth of turning point is –311 m in experiment E1, –293 m in experiment E4 and –273 m in experiment E5. Compared with experiment E1, the depths of turning point in experiments E4 and E5 were reduced by 5.79% and 12.22%, respectively. Thirdly, the horizontal baroclinic velocity decreased in the upper and lower layers of the pycnocline (Figs 7b–d).

3.3 *Influence of westward shoaling isopycnal slope angle (E7, E1 and E6)*

The influence of the isopycnal slope angle was analyzed by comparing the results in experiments E*i* (*i*=7, 1, 6) in Fig. 8. Firstly, it showed that when the isopycnal slope angle was in-

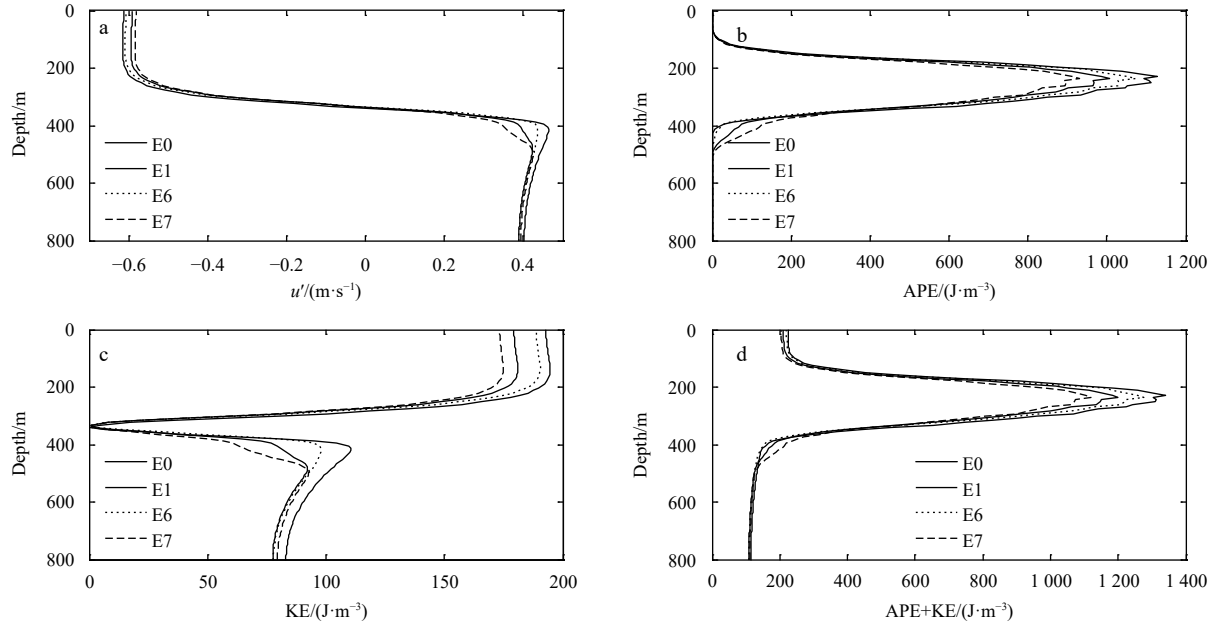

Fig. 8. Comparison of the model results along the dashed line section denoted in Fig. 5 in experiments E*i* (*i*=0, 1, 6, 7). a. Horizontal baroclinic velocity *u*′ vs. depth; b. APE densities vs. depth; c. KE densities vs. depth; d. APE+KE vs. depth.

creased by reducing R from 140 km in experiment E7 to 100 km in experiment E1 and 60 km in experiment E6, respectively, then the number of ISWs, phase speed of ISWs and total baroclinic energy in Packet A increased (Tables 2, 3 and Fig. 8). Similarly, Lien et al. (2012) also found that shoaling of a single deep-water ISW could also cause a train of smaller ISWs due to wave fission and dissipation. Secondly, the depth of turning point remained almost unchanged (Fig. 8), which might be caused by little change in water stratification. Thirdly, the horizontal baroclinic velocity increased in the upper and lower layers of the pycnocline with the increase of the isopycnal slope angle (Fig. 8), since the westward shoaling isopycnal might be more conducive to the formation of the trapped cores, which can enhance the dissipation through transporting water mass horizontally (Lien et al., 2012).

3.4 *Influence of pycnocline depth (E9, E1 and E8)*

The influence of the pycnocline depth was investigated by comparing the results in experiments Ei (i=9, 1, 8) in Fig. 9. Firstly, it showed that when the vertical depth of westward shoaling pycnocline was reduced, the depth of isopycnal undergoing maximum displacement, phase speed of ISWs, ratio of baroclinic energy to barotropic energy and total baroclinic energy in Packet A decreased, whilst the ISW amplitude, total barotropic kinetic energy and ratio of KE to APE increased (Tables 2, 3 and Fig. 9). Secondly, the depth of turning point got shallower (Fig. 9), it is −332 m in experiment E9, −311 m in experiment E1 and −269 m in experiment E8. Compared with experiment E9, the depths of turning point in experiments E1 and E8 were reduced by 6.33% and 18.98%, respectively. Thirdly, the horizontal baroclinic velocity increased in the upper and lower of the depth of turning point with the reduced pycnocline depth (Fig. 9).

3.5 *Importance of different influencing factors (E1, E10–E13)*

Base on experiment E1, four more experiments Ei (i=10, 11, 12, 13), in which one of the different influencing factors is increased by 10% separately, are added to investigate the importance of different influencing factor (Table 1), i.e., compared with experiment E1, the pycnocline thickness was changed into 89.1 m in experiment E10, the density difference across the pycnocline was changed into 4.4 kg/m^3 in experiment E11, R was changed into 110 km in experiment E12, dl and dr were increased by 17.8 m in experiment E13. Table 4 shows the comparison of the amplitude of the leading soliton in ISW Packet A in experiments Ei (i=1, 10, 11, 12, 13) at the fourth tidal period. Compared with that in E1, the decreased amplitude of the leading soliton in ISW Packet A was 4.92 m, 13.12 m, 5.64 m and 11.27 m in experiments E10, E11, E12 and E13, respectively. It shows that, the density difference across the pycnocline is the most important influencing factor, for instance, the ratio of decreased amplitude in E11 when compared with E1 reached 7.47%, whose variation is the most significant in these four experiments Ei (i=10, 11, 12, 13), in turn, the vertical depth of westward shoaling pycnocline is the second most important influencing factor, since the ratio of decreased amplitude in E13 when compared with E1 reaches 6.42%, which variation is the second largest.

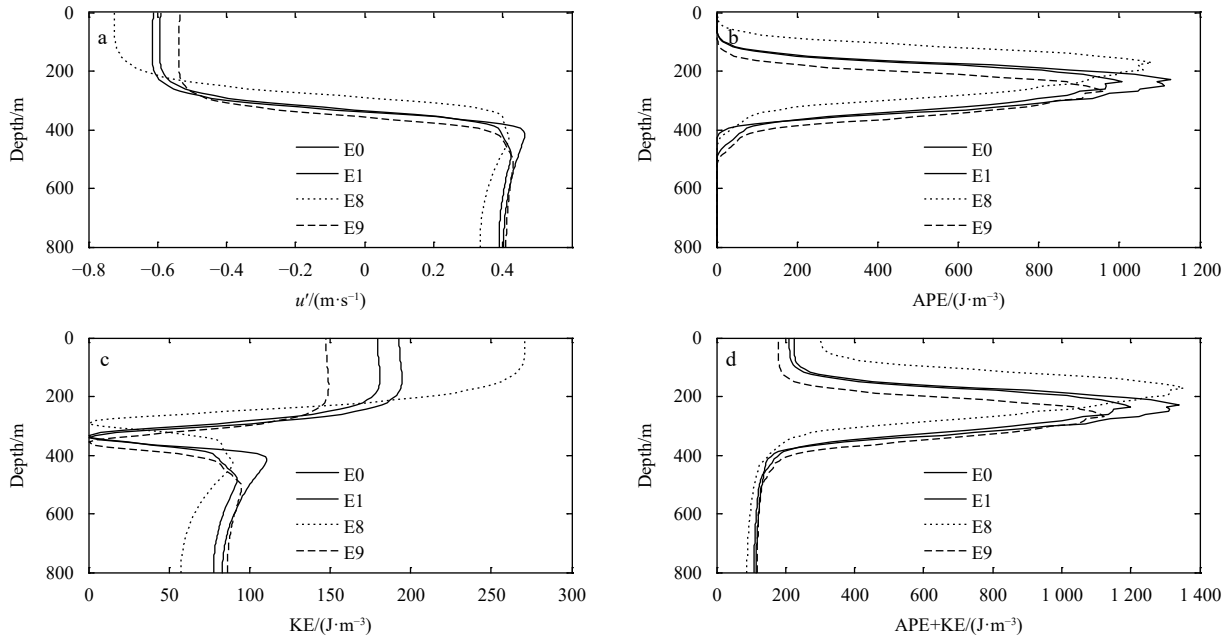

Fig. 9. Comparison of the model results along the dashed line section denoted in Fig. 5 in experiments Ei (i=0, 1, 8, 9). a. Horizontal baroclinic velocity u' vs. depth; b. APE densities vs. depth; c. KE densities vs. depth; d. APE+KE vs. depth.

Table 4. Comparison of the amplitude of the leading soliton in ISW Packet A in experiments Ei (i = 1, 10, 11, 12, 13) at 4T

	Experiment				
	E1	E10	E11	E12	E13
ISW amplitude η/m	175.54	170.62	162.42	169.90	164.27
Difference of amplitude between Ei and E1/m	–	4.92	13.12	5.64	11.27
Ratio of decreased amplitude in Ei when compared with E1/%	–	2.80	7.47	3.21	6.42

Note: – represents no data.

3.6 *Influence of westward shoaling pycnocline (E0, Ei (i=1, 2, ···, 13))*

A study of the effects of westward shoaling pycnocline stratification on ISWs is helpful for understanding the internal wave characteristics in the ocean. Figures 7–9 show the horizontal baroclinic velocity u', the baroclinic APE, KE and baroclinic energy densities vs. depth along the dashed lines in Fig. 5. It is clear that (1) the depth of turning point, where the horizontal current in upper layer began to turn to zero and flowed against that in lower layer, was at z=−317.65 m in experiment E0, which changed shallower with the westward shoaling pycnocline, except in experiment E9; (2) the horizontal baroclinic velocity decreased in the upper and lower layers of the pycnocline except in experiment E8, which might be caused by the shallowest pycnocline in experiment E8; (3) according to the results in Tables 2 and 3, the number of ISWs, total barotropic kinetic energy and baroclinic energy in wave Packet A all decreased with the westward shoaling pycnocline, yet the ratio of KE to APE increased. The energy decrease in ISWs due to the westward shoaling pycnocline might be because the westward shoaling pycnocline could form trapped cores to enhance the dissipation through transporting water mass horizontally and mix them with the background water (Lien et al., 2012).

3.7 *Depth integrated baroclinic energy in Packet A from 3T to 4.5T*

To study the temporal variation of the baroclinic energy in wave Packet A through the westward shoaling pycnocline, the baroclinic energy in the ISW Packet A from 3T to 4.5T was calculated (Fig. 10). Firstly, it showed that due to the westward shoaling pycnocline, the baroclinic energy in the wave Packet A decreased prominently in experiments Ei (i=1, 2, ···, 9), the maximum baroclinic energy was 1.50 MJ/m (0.48 MJ/m) in experiment E9 (E5). Secondly, the baroclinic energy decreased reversely with increased pycnocline thickness, e.g., compare experiments E1, E2 and E3. Thirdly, the baroclinic energy decreased with density difference across the pycnocline, e.g., compare experiments E1, E4 and E5. Fourthly, the baroclinic energy increased with isopycnal slope angle, and the ISW packet became steady more quickly with a greater isopycnal slope angle, e.g., compare experiments E1, E6 and E7. Finally, the total baroclinic energy decreased when the vertical depth of westward shoaling pycnocline, e.g., compare experiments E9, E1 and E8.

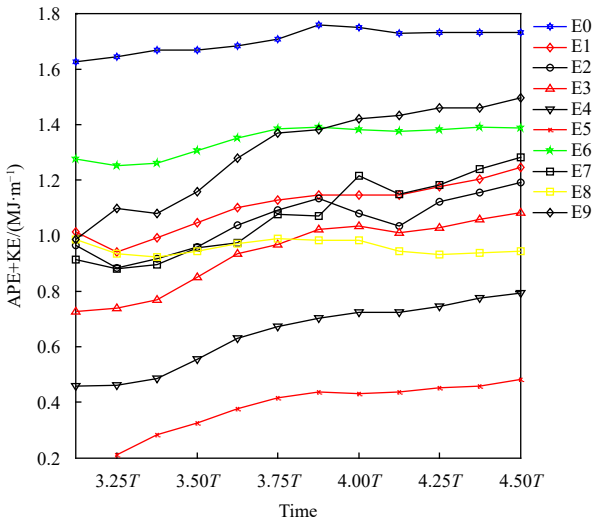

Fig. 10. Time series of the baroclinic energy in ISW Packet A from 3T to 4.5T for experiments Ei (i=0, 1, ···, 9).

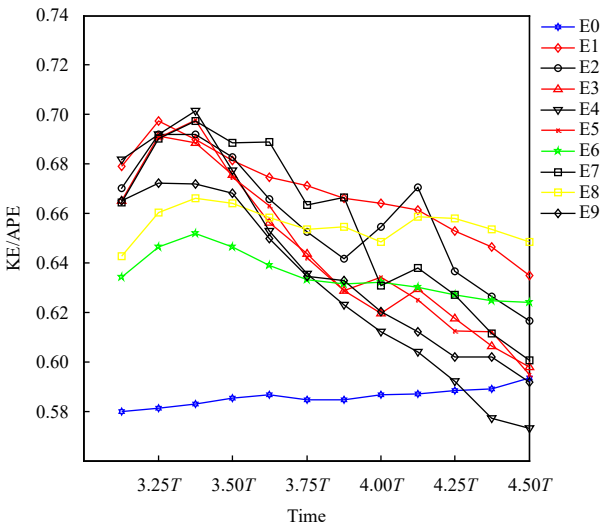

Fig. 11. Time series of the KE/APE in ISW Packet A from 3T to 4.5T for experiments Ei (i=0, 1, ···, 9).

The time series of the KE/APE in experiments Ei (i=0, 1, ···, 9) are shown in Fig. 11. It demonstrated that the KE/APE became steady ranging from 0.58 to 0.60 in experiment E0; however, the trends of KE/APE in experiments Ei (i=1, 2, ···, 9) changed dramatically, which ascended to a maximum at first, and then dropped gradually.

4 Conclusions

Fourteen experiments were designed to study the impacts of westward shoaling pycnocline on characteristics and energetics of ISWs by numerical simulations. The conclusions are as follows.

(1) With the westward shoaling pycnocline, the horizontal baroclinic velocity in the upper and lower layers of the pycnocline, the number of ISWs, total barotropic kinetic energy and baroclinic energy decreased. Moreover, the ratio of the KE to APE increased to a maximum at first, and then decreased gradually.

(2) When the pycnocline thickness on both sides of the sill increased synchronously, the ISW amplitude, number of ISWs, phase speed of ISWs, total barotropic kinetic energy, total baroclinic energy and ratio of KE to APE decreased, while the depth of isopycnal undergoing maximum displacement and ratio of baroclinic energy to barotropic energy increased.

(3) When the density difference across the pycnocline on both sides of the sill decreased synchronously, the ISW amplitude, phase speed of ISWs, total barotropic kinetic energy, ratio of baroclinic energy and barotropic energy and total baroclinic energy decreased, while the depth of isopycnal undergoing maximum displacement increased. When the density difference was reduced with the values of 4 kg/m^3, 3 kg/m^3 and 2.5 kg/m^3, the depths of turning point of the latter two was reduced by 5.79% and 12.22% respectively.

(4) When the westward shoaling isopycnal slope angle increased, the number of ISWs, phase speed of ISWs and total baroclinic energy increased, although the depth of turning point remained nearly unchanged. It was clearly noticed that the ISW packet became steady more quickly with a greater isopycnal slope angle.

(5) When the depth of westward shoaling pycnocline on both sides of the sill reduced synchronously, the depth of turning point, depth of isopycnal undergoing maximum displacement, phase speed of ISWs, ratio of baroclinic energy to barotropic energy and total baroclinic energy decreased, whilst the ISW amplitude, total barotropic kinetic energy and ratio of KE to APE increased.

(6) Compared with experiment E1, when only one of the above four different influencing factors was increased by 10%, the amplitude of the leading soliton in ISW Packet A was decreased by 2.80%, 7.47%, 3.21% and 6.42% in experiments E*i* (*i*=10, 11, 12, 13) respectively. The density differences across the pycnocline and the vertical depth of westward shoaling pycnocline are the two most important factors affecting the characteristics and energetics of ISWs.

Acknowledgements

Thanks to Lamb K G for providing the IGW model.

References

Bai Xiaolin, Li Xiaofeng, Lamb K G, et al. 2017. Internal solitary wave reflection near Dongsha Atoll, the South China Sea. Journal of Geophysical Research: Oceans, 122(10): 7978–7991, doi: 10.1002/2017JC012880

Boyer T, Levitus S. 1994. Quality control and processing of historical oceanographic temperature, salinity, and oxygen data. Washington, DC: US Department of Commerce, National Oceanic and Atmospheric Administration, 1–64

Buijsman M C, McWilliams J C, Jackson C R. 2010. East-west asymmetry in nonlinear internal waves from Luzon Strait. Journal of Geophysical Research: Oceans, 115(C10): C10057, doi: 10.1029/2009JC006004

Cai Shuqun, Long Xiaomin, Dong Danpeng, et al. 2008. Background current affects the internal wave structure of the northern South China Sea. Progress in Natural Science, 18(5): 585–589, doi: 10.1016/j.pnsc.2007.11.019

Cao Anzhou, Guo Zheng, Lv Xianqing, et al. 2017. Coherent and incoherent features, seasonal behaviors and spatial variations of internal tides in the northern South China Sea. Journal of Marine Systems, 172: 75–83, doi: 10.1016/j.jmarsys.2017.03.005

Chen Chenyuan, Hsu J R C, Cheng M H, et al. 2007. An investigation on internal solitary waves in a two-layer fluid: propagation and reflection from steep slopes. Ocean Engineering, 34(1): 171–184, doi: 10.1016/j.oceaneng.2005.11.020

Chen Zhiwu, Xie Jieshuo, Wang Dongxiao, et al. 2014. Density stratification influences on generation of different modes internal solitary waves. Journal of Geophysical Research: Oceans, 119(10): 7029–7046, doi: 10.1002/2014JC010069

Chen Zhiwu, Xie Jieshuo, Xu Jiexin, et al. 2013. Energetics of nonlinear internal waves generated by tidal flow over topography. Ocean Modelling, 68: 1–8, doi: 10.1016/j.ocemod.2013.04.008

Chen Liang, Zheng Quanan, Xiong Xuejun, et al. 2018. A new type of internal solitary waves with a re-appearance period of 23 h observed in the South China Sea. Acta Oceanologica Sinica, 37(9): 116–118, doi: 10.1007/s13131-018-1252-y

DeCarlo T M, Karnauskas K B, Davis K A, et al. 2015. Climate modulates internal wave activity in the Northern South China Sea. Geophysical Research Letters, 42(3): 831–838, doi: 10.1002/2014GL062522

Du Tao, Tseng Y H, Yan Xiaohai. 2008. Impacts of tidal currents and Kuroshio intrusion on the generation of nonlinear internal waves in Luzon Strait. Journal of Geophysical Research: Oceans, 113(C8): C08015, doi: 10.1029/2007JC004294

Grimshaw R, Wang Caixia, Li Lan. 2016. Modelling of polarity change in a nonlinear internal wave train in Laoshan Bay. Journal of Physical Oceanography, 46(3): 965–974, doi: 10.1175/JPO-D-15-0136.1

Huang Xiaodong, Zhao Wei, Tian Jiwei, et al. 2014. Mooring observations of internal solitary waves in the deep basin west of Luzon Strait. Acta Oceanologica Sinica, 33(3): 82–89, doi: 10.1007/s13131-014-0416-7

Lamb K G. 2008. On the calculation of the available potential energy of an isolated perturbation in a density-stratified fluid. Journal of Fluid Mechanics, 597: 415–427, doi: 10.1017/S0022112007009743

Lamb K G. 2010. Energetics of internal solitary waves in a background sheared current. Nonlinear Processes in Geophysics, 17(5): 553–568, doi: 10.5194/npg-17-553-2010

Lamb K G, Kim J. 2012. Conversion of barotropic tidal energy to internal wave energy over a shelf slope for a linear stratification. Continental Shelf Research, 33: 69–88, doi: 10.1016/j.csr.2011.11.005

Li Xiaofeng, Jackson C R, Pichel W G. 2013. Internal solitary wave refraction at Dongsha Atoll, South China Sea. Geophysical Research Letters, 40(12): 3128–3132, doi: 10.1002/grl.50614

Lien R C, D'Asaro E A, Henyey F, et al. 2012. Trapped core formation within a shoaling nonlinear internal wave. Journal of Physical Oceanography, 42(4): 511–525, doi: 10.1175/2011JPO4578.1

Liu Zihua, Grimshaw R, Johnson E. 2017. Internal solitary waves propagating through variable background hydrology and currents. Ocean Modelling, 116: 134–145, doi: 10.1016/j.ocemod.2017.06.008

Lü Haibin, Xie Jieshuo, Yao Yuan, et al. 2016. Effect of background parabolic current on characteristics and energetics of internal solitary waves by numerical simulation. Acta Oceanologica Sinica, 35(1): 1–10, doi: 10.1007/s13131-016-0790-4

Osborne A R, Burch T L. 1980. Internal solitons in the Andaman Sea. Science, 208(4443): 451–460, doi: 10.1126/science.208.4443.451

Park J H, Farmer D. 2013. Effects of Kuroshio intrusions on nonlinear internal waves in the South China Sea during winter. Journal of Geophysical Research: Oceans, 118(12): 7081–7094, doi: 10.1002/2013JC008983

Vázquez A, Bruno M, Izquierdo A, et al. 2008. Meteorologically forced subinertial flows and internal wave generation at the main sill of the Strait of Gibraltar. Deep Sea Research Part I: Oceanographic Research Papers, 55(10): 1277–1283, doi: 10.1016/j.dsr.2008.05.008

Wang Gang. 2006. Numerical modelling on the generation process of the tidal internal waves over the northwestern South China Sea shelf (in Chinese)[dissertation]. Qingdao: Institute of Oceanology, Chinese Academy of Sciences

Wang Juan, Huang Weigen, Yang Jingsong, et al. 2012. Study of the propagation direction of the internal waves in the South China Sea using satellite images. Acta Oceanologica Sinica, 32(5): 42–50

Xie Jieshuo, He Yinghui, Chen Zhiwu, et al. 2015. Simulations of internal solitary wave interactions with mesoscale eddies in the northeastern South China Sea. Journal of Physical Oceanography, 45(12): 2959–2978, doi: 10.1175/JPO-D-15-0029.1

Xu Zhenhua, Liu Kun, Yin Baoshu, et al. 2016. Long-range propagation and associated variability of internal tides in the South China Sea. Journal of Geophysical Research: Oceans, 121(11): 8268–8286, doi: 10.1002/2016JC012105

Zhao Zhongxiang. 2014. Internal tide radiation from the Luzon Strait. Journal of Geophysical Research: Oceans, 119(8): 5434–5448, doi: 10.1002/2014JC010014

Zheng Quanan, Song Y T, Lin Hui, et al. 2008. On generation source sites of internal waves in the Luzon Strait. Acta Oceanologica Sinica, 27(3): 38–50

Zheng Quanan, Susanto R D, Ho C R, et al. 2007. Statistical and dynamical analyses of generation mechanisms of solitary internal waves in the northern South China Sea. Journal of Geophysical Research: Oceans, 112(C3): C03021, doi: 10.1029/2006JC003551

Zheng Quanan, Susanto R D, Yan Xiaohai, et al. 1998. Observation of equatorial Kelvin solitary waves in a slowly varying thermocline. Nonlinear Processes in Geophysics, 5: 153–165, doi: 10.5194/npg-5-153-1998